ISOTOPE STRATIGRAPHY

143-million-year seawater osmium isotopic record: Trends, rhythms, and dynamics of volcanism and tectonics

Hironao Matsumoto[1,2]*, Yasuto Watanabe[3]*, Rodolfo Coccioni[4], Fabrizio Frontalini[5], Toshihiro Yoshimura[2], Junichiro Kuroda[6], Katsuhiko Suzuki[2,7]

Tectonic events and volcanic pulses forming large igneous provinces (LIPs) have altered Earth's paleoclimate. Osmium (Os) and strontium (Sr) isotopic ratios are key tracers of past continental weathering and LIP eruptions. However, limited Cretaceous seawater Os and riverine Os–Sr data have hindered quantitative reconstructions. In this study, we present a long-term Os isotopic record from the Cretaceous to the present, revealing ~10– to 20–million-year cycles during the Cretaceous that align with rhythmic LIP eruptions. Seawater Os–Sr isotopic trends indicate transitions in continental weathering patterns during the Late Cretaceous [~90 million years ago (Ma)] and Paleogene (~35 Ma) ascribed to intensified weathering of interior Gondwana during the opening of the Atlantic Ocean and the uplift and glaciation of the Himalaya, respectively. Our Os isotopic record highlights its utility in tracing long-term LIP cycles and identifying major paleogeographic turning points.

Throughout the Phanerozoic, Earth's climate and biosphere have been continuously transformed by intensive volcanic and tectonic episodes. In particular, from the Early Cretaceous [~143 million years ago (Ma)] to present day, mantle plume magmatism has formed numerous large igneous provinces (LIPs) (e.g., Paraná-Etendeka, Ontong Java Nui, Caribbean Plateau), and several major plate tectonic events (e.g., the breakup of Gondwana, Himalayan uplift) have occurred. These events are thought to have triggered episodic environmental perturbations, such as large-scale burial of organic carbon (e.g., oceanic anoxic events, OAEs) and extinctions of marine biota as well as long-term climatic trends, including mid-Cretaceous supergreenhouse and Neogene cooling (*1*–*3*).

Seawater osmium isotopic ratios ($^{187}Os/^{188}Os$) are influenced by changes in continental weathering patterns and volcanic events because they reflect the balance between radiogenic Os input from continental material ($^{187}Os/^{188}Os \sim 1.5$) and unradiogenic Os input from the mantle and extraterrestrial materials ($^{187}Os/^{188}Os \sim 0.12$) (*4*). Previous studies have used past seawater $^{187}Os/^{188}Os$ along with $^{87}Sr/^{86}Sr$ to investigate intervals of LIP activity and continental weathering (*5*–*9*). However, the paucity of Cretaceous Os isotopic data and paleoriverine Os and Sr isotopic compositions has prevented reliable estimation of long-term LIP and paleogeographic trends.

In this study, we collected and analyzed sedimentary rocks from three sites: (i) Deep-Sea Drilling Project (DSDP) Site 463, drilled in the Mid-Pacific Mountains; (ii) Ocean Drilling Program (ODP) Sites 762C and 763B, drilled in the Exmouth Plateau, Indian Ocean; and (iii) the Umbria-Marche Basin, central Italy (Fig. 1 and figs. S1 to S7). By applying the inverse aqua regia digestion method to these samples, we reconstructed seawater $^{187}Os/^{188}Os$ ratios from the Tithonian (latest Jurassic) to Barremian (Early Cretaceous) and from Coniacian to Maastrichtian (Late Cretaceous Cretaceous) (supplementary materials). Based on the age model of Geologic Time Scale 2020 (*10*), we combined these records with previously published $^{187}Os/^{188}Os$ data (see supplementary materials and data S1 to S3) to provide a long-term Os isotopic record from the base of Cretaceous to the present (Fig. 2). We observed cyclic variations of Cretaceous seawater $^{187}Os/^{188}Os$ ratios over periods of ~10 to 20 million years, which we interpret as reflecting the long-term cyclicity of volcanic pulses associated with LIP eruptions. Additionally, by combining Os and Sr isotopic values, we highlight shifts in continental weathering patterns during the Late Cretaceous (~90 Ma, potentially associated with the opening of the Atlantic Ocean) and the late Paleocene (~35 Ma, related to the Himalayan uplift and glaciations).

Rhythmic Os isotopic variations triggered by LIP eruptions

The steady increase in Neogene-Quaternary $^{187}Os/^{188}Os$ ratios has been linked to enhanced continental weathering associated with Himalayan uplift and glaciations as well as the weakening of hydrothermal activity, as indicated by increased seawater Mg/Ca ratios and a $^{87}Sr/^{86}Sr$ shift toward unradiogenic values (Fig. 2) (*11*–*15*). Paleogene $^{187}Os/^{188}Os$ ratios exhibit several sharp declines associated with extraterrestrial inputs due to the Popigai and Chesapeake (~35 Ma) and Chicxulub (~66 Ma) impact events (Fig. 2). There is a large Os isotopic shift toward unradiogenic values around 34.7 Ma, interpreted to reflect the weathering of ophiolite (*16*, *17*) or long-term interplanetary dust input (*18*). Although the radiometric ages of the Afar LIP overlap with this Os isotopic shift, the age of its peak is younger than those of the Os isotopic shifts (*19*, *20*), and further studies are necessary to determine the influence of Afar LIP volcanism on the marine Os cycle.

In contrast to the Cenozoic record, our new compilation highlights that Cretaceous Os isotopic ratios varied cyclically between 0.4 and 0.8 over periods of ~10 to 20 million years (Fig. 2), which is evident in wavelet analysis (fig. S8). Notably, we observed five broad (>1 million years; amplitude > 0.1) Os isotopic excursions toward unradiogenic values during the Cretaceous and early Paleocene (black bracketed lines, Fig. 2), namely during the Valanginian (Cre-Os1, ~133 Ma), Aptian (Cre-Os2, 120 to 113 Ma), late Albian (Cre-Os3, ~103 to 108 Ma), Turonian-Santonian (Cre-Os4, ~94 to 85 Ma), and Maastrichtian-Danian (Cre-Os5, 72 to 56 Ma). Some of the broad segments include shorter-term excursions (red bars, Fig. 2).

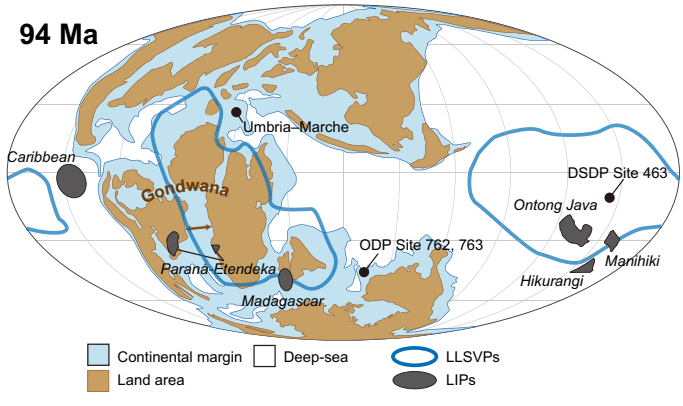

Fig. 1. Paleogeographic reconstruction for the Late Cretaceous (94 Ma). The locations of the sampling sites, LIPs, and LLSVPs are shown. The map is based on GPlates software (*65*).

[1]Institute of Life and Environmental Sciences, University of Tsukuba, Ibaraki, Japan. [2]Japan Agency for Marine-Earth Science and Technology, Kanagawa, Japan. [3]Earth System Division, National Institute for Environmental Studies, Ibaraki, Japan. [4]University of Urbino Carlo Bo, Urbino, Italy. [5]Department of Pure and Applied Sciences, University of Urbino Carlo Bo, Urbino, Italy. [6]Atmosphere and Ocean Research Institute, The University of Tokyo, Chiba, Japan. [7]Graduate School of Symbiotic Systems Science and Technology, Fukushima University, Fukushima, Japan. ***Corresponding author. Email: matsumoto.hironao.gw@u.tsukuba.ac.jp (H.M.); watanabe.yasuto@nies.go.jp (Y.W.)**

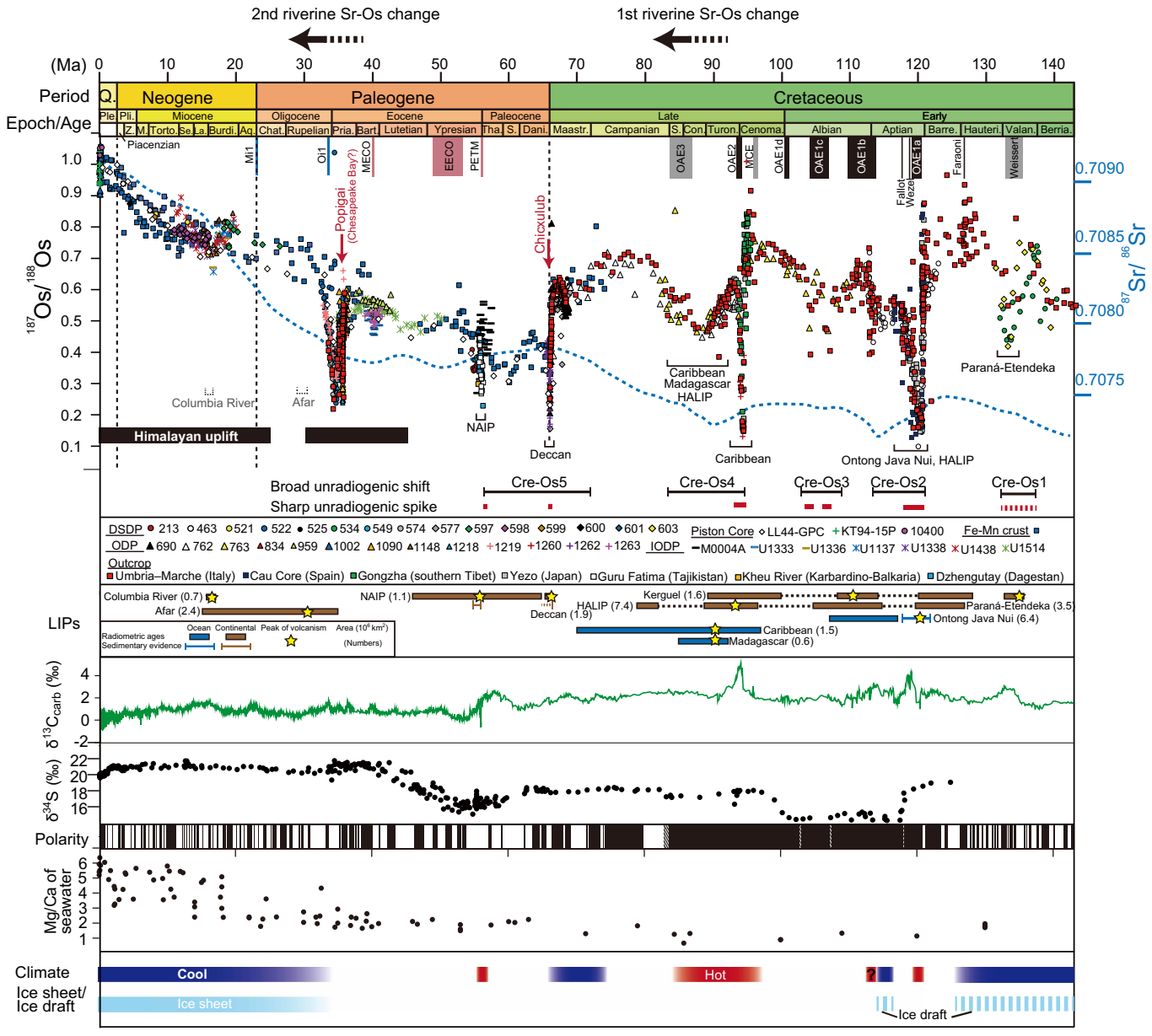

Fig. 2. Compilation of seawater Os and Sr isotopic ratios over the past 143 million years. Os isotopic data sources and LIP ages are available in the supplementary materials. Strontium isotopic data are from Geologic Time Scale 2020 (*66*). Carbon isotopic data and magnetic polarity were created using Time Scale Creator 8.0 (*67*). $\delta^{34}S$ values are from Paytan *et al*. (*68*), and Seawater Mg/Ca ratios are from Gothmann *et al*. (*14*). Climate data are from Leckie *et al*. (*1*) and Huber *et al*. (*2*). LIP eruptions are annotated below the Os and Sr trends (NAIP, North Atlantic Igneous Province; HALIP; High Arctic Large Igneous Province). Black bracketed lines (Cre-Os1 to Cre-Os5) represent broad (>1 million years) major Os isotopic excursions to unradiogenic values, with an amplitude larger than 0.1. Red bars indicate sharp Os isotopic shifts to unradiogenic values that are unaccompanied by Sr isotopic declines. Red arrows indicate major asteroid impacts. Bars at the top of the plot indicate the occurrence and timespan of oceanic anoxic events, global warming events, and cooling events. References for Os isotopic values and LIP ages are described in the supplementary materials. Berria., Berriasian; Valan., Valanginian; Hauteri., Hauterivian; Barre., Barremian; Cenoma., Cenomanian; Turon., Turonian; Con., Coniacian; S. in "Late Cretaceous," Santonian; Maastr., Maastrichtian; Dani., Danian; S. in "Paleocene," Selandian; Tha., Thanetian; Bart., Bartonian; Pria., Priabonian; Chat., Chattian; Aq., Aquitanian; Burdi., Burdigalian; La., Langhian; Se., Serravallian; Torto., Tortonian; M., Messinian; Z., Zanclean; Pli., Pliocene; Ple., Pleistocene; Q., Quaternary.

These five Os isotopic excursions to unradiogenic values could reflect the long-term cycle of LIP eruptions because they are accompanied by several sharp unradiogenic shifts to mantle values (red bars, Fig. 2) and correspond to the radiometric ages of LIP basalts (*5*, *6*, *21*, *22*). Indeed, Cre-Os1 and Cre-Os2 have been ascribed to volcanism associated with the Paraná-Etendeka LIP in the South Atlantic and Ontong Java Nui in the Pacific, respectively, based on their coincidence with radiometric ages of basaltic rocks and sedimentary evidence, such as volcanic ash interbeds (Figs. 1 and 2) (*6*, *7*, *23*–*25*). Cre-Os4 was also ascribed to LIP volcanism because its onset is marked by a dramatic Os isotopic decline at ~94 Ma (red bar in Cre-Os4, Fig. 2) and overlaps with the peak radiometric ages of several LIPs (Caribbean Plateau, Madagascar LIP, and High Arctic Large Igneous Provinces) (Fig. 1) (*21*). Cre-Os5 is broader and more gradual than the other excursions but includes distinct unradiogenic shifts related to the Deccan Traps (~66 Ma) (*26*) and the North Atlantic Igneous Province (*27*).

Potential mechanism for mantle-derived Os emissions during LIP eruptions

Two long-term Os isotopic trends during the Aptian (Cre-Os2) and Turonian-Santonian (Cre-Os4) may be well explained by protracted

hydrothermal activity and basalt weathering associated with LIP activity (Fig. 2). Indeed, these Os isotopic excursions correspond to decreased $^{87}Sr/^{86}Sr$ (*28*), a well-established proxy for hydrothermal activity and basalt weathering (*29*–*31*). By contrast, sharp Os isotopic drops during the Valanginian (Cre-Os1), earliest Aptian (red bar in Cre-Os2), late Albian (Cre-Os3), and end-Cenomanian (red bars in Cre-Os4), which define 10– to 20–million-year cycles, are accompanied by very small or no apparent declines in $^{87}Sr/^{86}Sr$ (Fig. 2 and fig. S8). Specifically, the Os isotopic shift during the OAE1a, attributed to Ontong Java volcanism, requires substantial mantle-derived Os input [equivalent to at least 30% of Os contained in the Ontong Java Plateau (OJP); (*6*)], although no comparable Os depletion in the OJP basalts has been reported. Therefore, in addition to hydrothermal and basalt weathering processes, another mechanism capable of preferentially releasing Os is likely required to explain these episodes.

We propose that these sharp $^{187}Os/^{188}Os$ shifts to unradiogenic values, without a corresponding decline in $^{87}Sr/^{86}Sr$, may have been triggered by enhanced upwelling of oxidized mantle plumes and the resulting oxidation of Os into volatile forms. LIPs are known to originate from mantle plumes arising from the edges of large low-shear-velocity provinces (LLSVPs; hot, dense provinces in the lower mantle) beneath Africa and the southern Pacific Ocean (Fig. 1) (*32*). Indeed, all Cretaceous LIPs associated with ~10– to 20–million-year cyclic Os isotopic variations lie vertically above or near LLSVP margins (Fig. 1). Geodynamic models have shown that oceanic slabs subducting beneath the Pangean supercontinent pushed thermal boundary layers upward along the LLSVP margin, triggering the upwelling of mantle plumes during the Paleozoic and eventually leading to Cretaceous LIP eruptions (*32*–*36*). LLSVPs may be enriched in Fe^{3+}-rich bridgmanite and are more oxidized than the surrounding lower mantle (*37*); therefore, cyclic mantle plume upwellings from LLSVPs may have promoted the oxidation of Os into volatile forms. This process could have enhanced the mobility of Os and released large amounts of mantle-derived Os into the ocean, potentially leading to repeated sharp Os isotopic declines through active volcanic degassing (*38*–*40*). For example, in the case of the OJP, some mantle xenoliths are extremely depleted in Os [~100 parts per trillion (ppt)] compared with other xenoliths (~3 to 5 parts per billion), suggesting substantial Os loss during the OJP eruption, potentially through volatilization processes (*24*, *41*). By contrast, Sr does not have strong volatility with oxidation, and the major Sr emission process could have been hydrothermal activity and/or weathering of basaltic rocks. Therefore, we propose that increased Os emission without associated Sr isotopic excursion may represent the input of unradiogenic Os through volatile forms (red bars, Fig. 2).

Sharp Os isotopic shifts to unradiogenic values could be associated with emissions of other volatile elements, such as CO_2 and SO_2. Indeed, Os isotopic shifts during the early to mid-Aptian OAEs and Paleocene-Eocene Thermal Maximum (PETM) are accompanied by negative carbon isotopic excursions, implying the input of volcanic carbon (*7*, *25*, *42*). Considering that negative shifts are less pronounced in other events (e.g., Valanginian Weissert Event and end-Cenomanian OAE2), the balance between volcanic degassing and organic carbon burial could have played an important role in generating carbon isotopic shifts. Sulfur could also reflect signals of volcanic degassing. Although sulfur isotope ratios exhibit a negative shift during OAE1a, comparable fluctuations are not evident in other events (*43*), possibly because the amount of sulfur release was insufficient to produce detectable changes in seawater sulfur isotopic composition.

Combining Os and other volatile information, we suggest that Cretaceous seawater Os isotopic variations resulted from two processes associated with LIP eruptions: long-term mantle-derived Os input associated with conventional hydrothermal activity and basalt weathering and episodic inputs associated with the oxidation of Os into volatile form.

It is important to note that the magnitude of Os isotopic shifts does not necessarily correlate with the size of LIPs (Fig. 2). Indeed, Os isotopic variations tend to be larger and more abrupt during submarine LIP eruptions (e.g., Ontong Java and Caribbean Plateaus) than during subaerial events (e.g., Kerguelen Plateau, North Atlantic Igneous Province, Columbia River Basalts), possibly because submarine eruptions release unradiogenic Os directly into the ocean. Additionally, the oxygen fugacity of the mantle plume may also influence the Os emission rate. Therefore, a better understanding of Os emission processes is essential to clarify the relationship between LIP size and its impact on the marine Os cycle.

Temporal changes in riverine Os and Sr isotopic values

With the exception of periods affected by large asteroid impacts and some LIP eruptions (red bars, Fig. 2), seawater Os and Sr isotopic ratios seem to have covaried (*7*, *44*) over longer timescales (>25 million years). Indeed, both $^{187}Os/^{188}Os$ and $^{87}Sr/^{86}Sr$ records show a distinct radiogenic shift during the Neogene and Quaternary (Figs. 2 and 3). Assuming present-day riverine Os and Sr isotopic values of $^{187}Os/^{188}Os = 1.54$ (supplementary materials) and $^{87}Sr/^{86}Sr = 0.71106$ (*45*), the Neogene-Quaternary trend can be explained by a steady increase in the continental weathering rate and/or a decrease in the supply of mantle-derived materials (blue mixing lines, Fig. 3; see supplementary materials). Early to mid-Cretaceous isotopic trends appear more complicated owing to smaller Sr isotopic variations compared with those of the Neogene-Quaternary as well as several sharp Os isotopic shifts to unradiogenic values. However, they roughly fluctuate between radiogenic ($^{187}Os/^{188}Os$ = ~0.7 to 0.8 and $^{87}Sr/^{86}Sr$ = ~0.7075) and unradiogenic ($^{187}Os/^{188}Os$ = ~0.4 to 0.5 and $^{87}Sr/^{86}Sr$ = ~0.7072) values (Figs. 2 and 3). Although the marine Os and Sr isotopic systems respond to different forcing mechanisms, marine $^{187}Os/^{188}Os$ and $^{87}Sr/^{86}Sr$ trends could have been coupled during

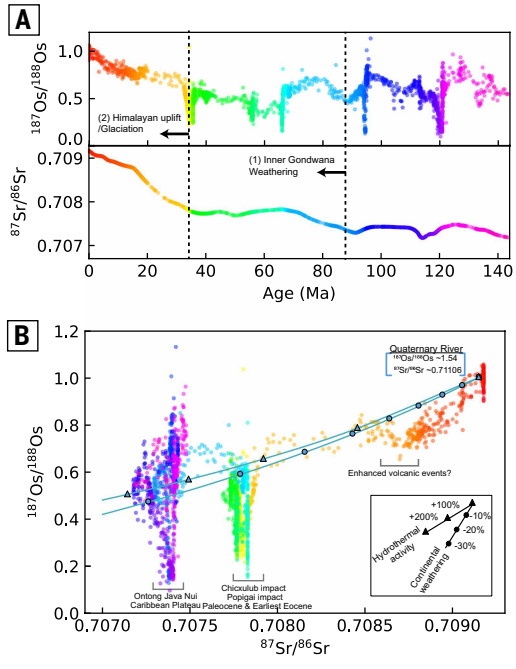

Fig. 3. Cross-comparisons of $^{87}Sr/^{86}Sr$ and $^{187}Os/^{188}Os$ values of seawater. (**A** and **B**) Cretaceous–Cenozoic seawater $^{87}Sr/^{86}Sr$ and $^{187}Os/^{188}Os$ records (A) and their cross plots (B) are shown. Sources of $^{187}Os/^{188}Os$ data are listed in supplementary materials. $^{87}Sr/^{86}Sr$ data are from Geologic Time Scale 2020 (*66*). Mixing lines denote expected values given endmember riverine compositions and indicated degrees of continental weathering and hydrothermal activity. Triangles represent the $^{87}Sr/^{86}Sr$ and $^{187}Os/^{188}Os$ values when the input rate of hydrothermally derived Os increases by 100% relative to present-day hydrothermal Os flux. Circles represent the $^{87}Sr/^{86}Sr$ and $^{187}Os/^{188}Os$ values when the input rate of continental Os decreased by 10% relative to present-day continental Os flux.

the Neogene-Quaternary and Early to mid-Cretaceous. The Cretaceous trend seems much steeper than those during the Neogene-Quaternary (Fig. 3), and most of the data are plotted above the Neogene-Quaternary mixing line; this difference cannot be fully explained by changes in mantle- or continent-derived Os and Sr fluxes alone.

In this study, we used a simple ocean box model to understand the long-term marine Os and Sr cycles. For the Os cycle, continental and hydrothermal Os fluxes were estimated from past variations in atmospheric pCO_2 and oceanic crustal production rates, respectively. Riverine Os isotopic values were fixed at 1.54 with ~10% uncertainties because the Cretaceous-Cenozoic tectonic changes (e.g., Gondwanan breakup and Himalayan uplift) likely had only a minor influence on riverine $^{187}Os/^{188}Os$ value (supplementary materials). Using these constraints and seawater Os isotopic records, we calculated temporal changes in LIP-derived Os flux (Os_{LIP}), which is the primary driver of Cretaceous Os isotopic fluctuations (Fig. 4).

For the Sr cycle, continental and hydrothermal Sr fluxes were estimated using the same approach as for Os. The Sr fluxes from LIP volcanism (Sr_{LIP}) were determined to mirror the Os_{LIP} variations. Lastly, from these constraints and seawater Sr isotopic variations, we calculated the changes in the riverine $^{87}Sr/^{86}Sr$ values, which can be strongly influenced by Cretaceous-Cenozoic tectonic changes (supplementary materials). We adopted $Os_{LIP}/Sr_{LIP} > 1 \times 10^{-7}$, higher than the Os/Sr ratio of typical basalts [~0.6×10^{-7}; (*15*)], because lower values result in unrealistically high Eocene riverine $^{87}Sr/^{86}Sr$ ratios (>0.72). Such high Os_{LIP}/Sr_{LIP} values are consistent with the hypothesis that LIP volcanism preferentially releases Os relative to Sr (*7*).

Our results indicate a strong influence of LIP-derived Os and Sr during the mid-Cretaceous and Eocene (red lines, Fig. 4). Furthermore, the riverine $^{87}Sr/^{86}Sr$ values shifted from ~0.710 to ~0.711 from the Late Cretaceous to the Neogene (Fig. 4D). Indeed, a similar increase in riverine $^{87}Sr/^{86}Sr$ ratios has also been inferred from past seawater Sr/Ca ratios (*46*). We consider that such variation in riverine $^{87}Sr/^{86}Sr$ is a plausible driver of the changes in the observed seawater $^{187}Os/^{188}Os$–$^{87}Sr/^{86}Sr$ trends.

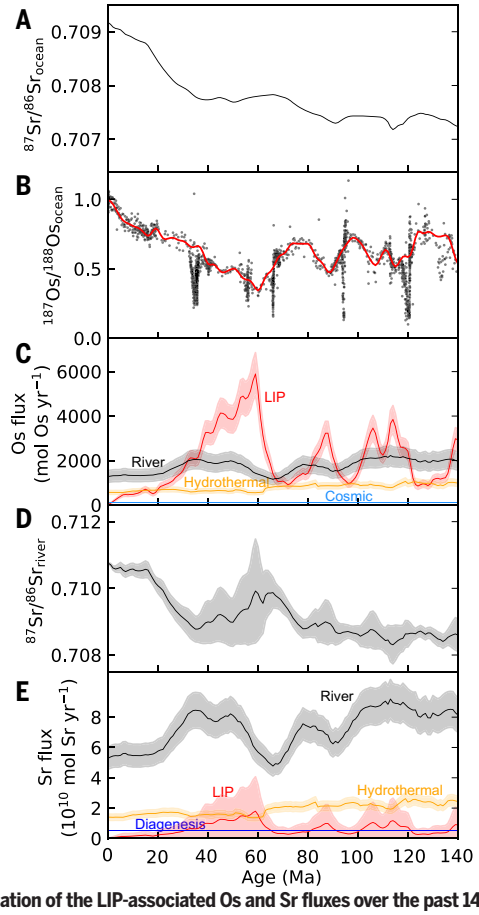

Fig. 4. Estimation of the LIP-associated Os and Sr fluxes over the past 140 million years. (**A** to **E**) The evolutions of marine Sr isotope records (black line) (A), marine Os isotope records (black dot) and the continuous long-term curve used as an input of the model (red line) (B), marine Os budget (black, riverine input; orange, hydrothermal input; light blue, cosmic input; red, unradiogenic Os flux associated with LIPs volcanism) (C), Sr isotope signature of riverine Sr input estimated by the model (D), and marine Sr budget (black, riverine input; orange, hydrothermal input; blue, diagenetic input; red, unradiogenic Sr flux associated with LIP volcanism) (E). The shaded regions shown in (C), (D), and (E) represent one standard deviation from the mean.

The Atlantic opening and Himalayan uplift caused shifts in marine elemental cycles

During the past 143 million years, marked shifts in seawater $^{187}Os/^{188}Os$–$^{87}Sr/^{86}Sr$ trends have occurred during two intervals: (i) the Late Cretaceous (~90 Ma), when seawater $^{187}Os/^{188}Os$ ratios began to shift toward unradiogenic values despite steadily rising $^{87}Sr/^{86}Sr$ ratios, and (ii) the latest Eocene (~35 Ma), when both $^{187}Os/^{188}Os$ and $^{87}Sr/^{86}Sr$ ratios shift synchronously toward more radiogenic values (Figs. 2 and 3). As inferred from the modeling calculations, such changes correspond to transitions in riverine $^{87}Sr/^{86}Sr$ values (Fig. 4D).

We propose that the Late Cretaceous shift in seawater $^{87}Sr/^{86}Sr$–$^{187}Os/^{188}Os$ trends (Figs. 2, 3, and 4) was potentially related to the widening of the equatorial and South Atlantic oceans. During the Early to mid-Cretaceous, precipitation and chemical weathering in the Gondwanan interior (Fig. 1) were likely very low owing to limited moisture influx from the semiclosed narrow Atlantic Ocean (*47*) and distant coastal areas (*48*). Furthermore, the scarcity of fresh, weatherable silicate minerals in the Gondwanan interior, resulting from the lack of major orogenic events and the widespread coverage by weathered materials [a transport-limited regime (*49*)], would have decreased silicate weathering efficiency, potentially resulting in persistently high pCO_2 levels. However, once the Atlantic widened during the Late Cretaceous, weathering in the inner part of Gondwana increased owing to enhanced precipitation (*47*, *48*). Additionally, increased precipitation and orogeny along the Andes and northeastern South America during the Campanian (*50*, *51*) could have actively removed weathered soils and supplied fresh silicate minerals to the Gondwanan interior [weathering-limited regime (*49*)], potentially enhancing the chemical fluxes from inner Gondwana to the ocean. Modern rivers draining eastern South America and western Africa are characterized by high $^{87}Sr/^{86}Sr$ values (*52*–*54*) and slightly low $^{187}Os/^{188}Os$ ratios (*4*); accordingly, such intensive weathering of the Gondwanan interior could have caused a radiogenic shift in riverine $^{87}Sr/^{86}Sr$ values and a small unradiogenic shift in riverine $^{187}Os/^{188}Os$ values, which may have caused the initial shift in seawater $^{187}Os/^{188}Os$–$^{87}Sr/^{86}Sr$ trends across the Cretaceous-Neogene transition. Although the Gondwanan breakup was a gradual process, the chemical alteration index, hafnium isotopes, and clay mineral compositions inferred an abrupt increase in chemical weathering across pan-Atlantic regions during the Late Cretaceous (*51*, *55*), supporting our inference that inner Gondwanan weathering could have started to influence global elemental cycles at this time. Because the mid-Cretaceous was characterized by long volcanic arcs (*56*), the reduced weathering of young felsic arc rocks may have also contributed to the shift in riverine $^{87}Sr/^{86}Sr$ values toward radiogenic values during the Late Cretaceous, whereas its influence on riverine $^{187}Os/^{188}Os$ values has been limited due to very low Os concentrations [~8 ppt (*57*)].

As debated in previous studies, the onset of the concerted radiogenic shift in seawater $^{187}Os/^{188}Os$–$^{87}Sr/^{86}Sr$ values since the latest Eocene corresponds to Himalayan uplift and the onset of glaciations (*15*, *58*, *59*). These geological events exposed radiogenic carbonate rocks, organic-rich

sediments, and old continental crust across the Himalaya and other high-latitude regions (*60*, *61*), ultimately leading to enhanced riverine Os and Sr fluxes, a radiogenic shift in riverine $^{87}Sr/^{86}Sr$ values (Figs. 3 and 4), and a slight radiogenic shift in riverine $^{187}Os/^{188}Os$ values (supplementary materials) (*59*, *62*). Himalayan orogenic activity continued for ~40 million years, but our study suggests that the important changes in seawater $^{87}Sr/^{86}Sr$–$^{187}Os/^{188}Os$ trends occurred at around the Eocene-Oligocene boundary, corresponding to the abrupt Himalayan uplift at this point (*63*). Furthermore, as shown by the modeling results, a continuous decline in mantle-derived Os and Sr inputs could have contributed to increasing seawater $^{87}Sr/^{86}Sr$–$^{187}Os/^{188}Os$ during the Neogene (Fig. 4).

Another potential mechanism for the Neogene Os isotopic shift is the exposure of continental shelves caused by a significant sea level fall associated with global cooling (*64*). On short timescales, this process would have eroded younger, less radiogenic sediments. Over longer timescales, however, the exposure of older basement rocks could have supplied radiogenic Os and Sr to the ocean, potentially leading to the Neogene seawater Os isotopic shift toward radiogenic values. Nevertheless, current knowledge of the exposed terrains remains insufficient to accurately quantify the corresponding changes in Os and Sr fluxes and their isotopic compositions.

We suggest that major geographic events during the Late Cretaceous and Cenozoic caused a radiogenic shift in riverine $^{87}Sr/^{86}Sr$ values and slight variations in $^{187}Os/^{188}Os$ values, ultimately leading to a change in $^{187}Os/^{188}Os$–$^{87}Sr/^{86}Sr$ trends across the Cretaceous-Cenozoic transition. Indeed, when contributions from the Himalaya, Arctic, and interior of Gondwana are reduced relative to present-day conditions, a hypothetical Cretaceous riverine $^{87}Sr/^{86}Sr$ becomes less radiogenic than its present-day value, whereas changes in $^{187}Os/^{188}Os$ are minor (supplementary materials). In addition, the reduction of mantle-derived Os and Sr input also contributed to the Neogene Os and Sr isotopic shift toward radiogenic values. Our long-term Os isotopic record offers insights not only into the cyclic nature of LIP activity over geological timescales but also into key turning points in Earth's paleogeographic evolution.

REFERENCES AND NOTES

1. R. M. Leckie, T. J. Bralower, R. Cashman, *Paleoceanography* **17**, 13-1–13-29 (2002).
2. B. T. Huber, K. G. MacLeod, D. K. Watkins, M. F. Coffin, *Global Planet. Change* **167**, 1–23 (2018).
3. M. E. Raymo, W. F. Ruddiman, *Nature* **359**, 117–122 (1992).
4. S. Levasseur, J. L. Birck, C. J. Allegre, *Earth Planet. Sci. Lett.* **174**, 7–23 (1999).
5. S. C. Turgeon, R. A. Creaser, *Nature* **454**, 323–326 (2008).
6. M. L. G. Tejada *et al.*, *Geology* **37**, 855–858 (2009).
7. H. Matsumoto *et al.*, *Geology* **49**, 1148–1152 (2021).
8. L. M. Percival *et al.*, *Geology* **44**, 759–762 (2016).
9. P. A. Pogge von Strandmann, H. C. Jenkyns, R. G. Woodfine, *Nat. Geosci.* **6**, 668–672 (2013).
10. A. S. Gale, J. Mutterlose, S. Batenburg, in *Geologic Time Scale 2020*, vol. 2, F. M. Gradstein, J. G. Ogg, M. Schmitz, G. Ogg, Eds. (Elsevier, 2020), pp. 1023–1085.
11. W. J. Pegram, S. Krishnaswami, G. E. Ravizza, K. K. Turekian, *Earth Planet. Sci. Lett.* **113**, 569–576 (1992).
12. S. K. Singh, J. R. Trivedi, S. Krishnaswami, *Geochim. Cosmochim. Acta* **63**, 2381–2392 (1999).
13. J. T. Chesley, J. Quade, J. Ruiz, *Earth Planet. Sci. Lett.* **179**, 115–124 (2000).
14. A. M. Gothmann *et al.*, *Geochim. Cosmochim. Acta* **160**, 188–208 (2015).
15. G. Li, H. Elderfield, *Geochim. Cosmochim. Acta* **103**, 11–25 (2013).
16. D. N. Reusch, *Geology* **39**, 807–810 (2011).
17. W. J. Pegram, K. K. Turekian, *Geochim. Cosmochim. Acta* **63**, 4053–4058 (1999).
18. F. S. Paquay, G. Ravizza, R. Coccioni, *Geochim. Cosmochim. Acta* **144**, 238–257 (2014).
19. Q. Jiang, F. Jourdan, H. K. Olierook, R. E. Merle, *Earth Sci. Rev.* **237**, 104314 (2023).
20. Y. Yoshimura *et al.*, *Geophys. Res. Lett.* **50**, e2022GL102560 (2023).
21. H. Matsumoto, A. Ishikawa, R. Coccioni, F. Frontalini, K. Suzuki, *Sci. Rep.* **13**, 22051 (2023).
22. L. M. E. Percival *et al.*, *Geology* **51**, 753–757 (2023).
23. R. Martínez-Rodríguez *et al.*, *Global Planet. Change* **207**, 103652 (2021).
24. H. Matsumoto *et al.*, *Commun. Earth Environ.* **5**, 155 (2024).
25. H. Matsumoto *et al.*, *Sci. Adv.* **11**, eadt0204 (2025).
26. N. Robinson, G. Ravizza, R. Coccioni, B. Peucker-Ehrenbrink, R. Norris, *Earth Planet. Sci. Lett.* **281**, 159–168 (2009).
27. A. J. Dickson *et al.*, *Palaeogeogr. Palaeoclimatol. Palaeoecol.* **438**, 300–307 (2015).
28. T. J. Bralower, P. D. Fullagar, C. K. Paull, G. S. Dwyer, R. M. Leckie, *Geol. Soc. Am. Bull.* **109**, 1421–1442 (1997).
29. F. Albarède, A. Michard, J. F. Minster, G. Michard, *Earth Planet. Sci. Lett.* **55**, 229–236 (1981).
30. M. R. Palmer, H. Elderfield, *Nature* **314**, 526–528 (1985).
31. A. Paytan *et al.*, *Science* **371**, 1346–1350 (2021).
32. K. Burke, B. Steinberger, T. H. Torsvik, M. A. Smethurst, *Earth Planet. Sci. Lett.* **265**, 49–60 (2008).
33. B. Steinberger, T. H. Torsvik, *Geochem. Geophys. Geosyst.* **13**, 2011GC003808 (2012).
34. J. Dannberg, R. Gassmöller, *Proc. Natl. Acad. Sci. U.S.A.* **115**, 4351–4356 (2018).
35. B. H. Heyn, C. P. Conrad, R. G. Trønnes, *J. Geophys. Res. Solid Earth* **125**, e2019JB018726 (2020).
36. P. J. Heron *et al.*, *Spec. Publ. Geol. Soc. Lond.* **542**, 105–128 (2024).
37. W. Wang *et al.*, *Nat. Commun.* **12**, 1911 (2021).
38. U. Krähenbühl, M. Geissbühler, F. Bühler, P. Eberhardt, D. L. Finnegan, *Earth Planet. Sci. Lett.* **110**, 95–98 (1992).
39. M. A. Yudovskaya *et al.*, *Chem. Geol.* **248**, 318–341 (2008).
40. A. Gannoun, I. Vlastélic, P. Schiano, *Geochim. Cosmochim. Acta* **166**, 312–326 (2015).
41. A. Ishikawa, D. G. Pearson, C. W. Dale, *Earth Planet. Sci. Lett.* **301**, 159–170 (2011).
42. M. Gutjahr *et al.*, *Nature* **548**, 573–577 (2017).
43. M. L. Gomes, M. T. Hurtgen, B. B. Sageman, *Paleoceanography* **31**, 233–251 (2016).
44. G. Ravizza, *Earth Planet. Sci. Lett.* **118**, 335–348 (1993).
45. B. Peucker-Ehrenbrink, G. J. Fiske, *Chem. Geol.* **510**, 140–165 (2019).
46. C. H. Lear, H. Elderfield, P. A. A. Wilson, *Earth Planet. Sci. Lett.* **208**, 69–84 (2003).
47. L. Burgener, E. Hyland, B. J. Reich, C. Scotese, *Palaeogeogr. Palaeoclimatol. Palaeoecol.* **613**, 111373 (2023).
48. Y. Hu *et al.*, *Nat. Geosci.* **16**, 1041–1046 (2023).
49. R. F. Stallard, J. M. Edmond, *J. Geophys. Res.* **88** (C14), 9671–9688 (1983).
50. E. Jaillard, *Earth Sci. Rev.* **230**, 104033 (2022).
51. P. Corentin *et al.*, *Mar. Geol.* **455**, 106968 (2023).
52. M. R. Palmer, J. M. Edmond, *Earth Planet. Sci. Lett.* **92**, 11–26 (1989).
53. R. V. Santos *et al.*, *Hydrol. Processes* **29**, 187–197 (2015).
54. G. Bayon *et al.*, *Chem. Geol.* **559**, 119958 (2021).
55. E. Chenot *et al.*, *Global Planet. Change* **162**, 292–312 (2018).
56. W. Cao, C. T. A. Lee, J. S. Lackey, *Earth Planet. Sci. Lett.* **461**, 85–95 (2017).
57. C. Koeberl, W. U. Reimold, S. B. Shirey, *Geochim. Cosmochim. Acta* **58**, 2893–2910 (1994).
58. S. Misra, P. N. Froelich, *Science* **335**, 818–823 (2012).
59. C. Wanner, E. L. Sonnenthal, X. M. Liu, *Chem. Geol.* **381**, 154–167 (2014).
60. F. M. Richter, D. B. Rowley, D. J. DePaolo, *Earth Planet. Sci. Lett.* **109**, 11–23 (1992).
61. E. Ownsworth *et al.*, *Quat. Sci. Rev.* **308**, 108082 (2023).
62. F. Mokadem *et al.*, *Earth Planet. Sci. Lett.* **415**, 111–120 (2015).
63. L. Ding *et al.*, *Nat. Rev. Earth Environ.* **3**, 652–667 (2022).
64. R. Oxburgh, A. C. Pierson-Wickmann, L. Reisberg, S. Hemming, *Earth Planet. Sci. Lett.* **263**, 246–258 (2007).
65. R. D. Müller *et al.*, *Geochem. Geophys. Geosyst.* **19**, 2243–2261 (2018).
66. J. M. McArthur, R. J. Howarth, G. A. Shields, Y. Zhou, in *Geologic Time Scale 2020*, **vol. 1**, F. M. Gradstein, J. G. Ogg, M. Schmitz, G. Ogg, Eds. (Elsevier, 2020), pp. 211–238.
67. J. Ogg, G. Ogg, F. Gradstein, Time Scale Creator 8.0 (2021); https://engineering.purdue.edu/Stratigraphy/tscreator.
68. A. Paytan, W. Yao, K. L. Faul, E. T. Gray, in *Geologic Time Scale 2020*, **vol. 1**, F. M. Gradstein, J. G. Ogg, M. Schmitz, G. Ogg, Eds. (Elsevier, 2020), pp. 259–278.

ACKNOWLEDGMENTS

We acknowledge T. Nozaki, Y. Otsuki, and J. Kikuchi for their assistance with Re-Os analysis. We thank B. Peucker-Ehrenbrink, A. Dickson, and an anonymous reviewer for their constructive comments. We thank J. M. McArthur for sharing the seawater $^{87}Sr/^{86}Sr$ data. Some of the samples used in this study were provided by the International Ocean Discovery Program (IODP; sample request numbers 075591IODP, 099144IODP, and 104705IODP). **Funding:** Grants-in-aid for a Japan Society for the Promotion of Science Research Fellow 22J00271 and 22KJ3196 (H.M.). **Author contributions:** Conceptualization: H.M., J.K., F.F.; Data curation: H.M., Y.W.; Resources: Y.W., R.C., F.F., T.Y., J.K., K.S.; Formal analysis: H.M., Y.W.; Methodology: H.M., Y.W., K.S.; Investigation: H.M., Y.W., T.Y.; Validation: H.M., Y.W.; Visualization: H.M., Y.W.; Funding acquisition: H.M., J.K., K.S.; Project administration: H.M.; Supervision: H.M., J.K., K.S.; Software: Y.W. Writing – original draft: H.M., F.F.; Writing – review & editing: Y.W., R.C., F.F., T.Y., J.K., K.S. **Competing interests:** The authors declare that they have no competing interests. **Data, code, and materials availability:** All data needed to evaluate the conclusions in the paper are present in the paper or the supplementary materials. The samples used in this study are available upon reasonable request.

SUPPLEMENTARY MATERIALS

science.org/doi/10.1126/science.adw8301
Materials and Methods; Figs. S1 to S9; Tables S1 and S2; References (*69*–*113*); Data S1 to S3

Submitted 17 February 2025; accepted 5 December 2025

10.1126/science.adw8301